NATURAL HAZARDS

Atmospheric waves and global seismoacoustic observations of the January 2022 Hunga eruption, Tonga

Robin S. Matoza[1]*, David Fee[2], Jelle D. Assink[3], Alexandra M. Iezzi[1], David N. Green[4], Keehoon Kim[5], Liam Toney[2], Thomas Lecocq[6], Siddharth Krishnamoorthy[7], Jean-Marie Lalande[8], Kiwamu Nishida[9], Kent L. Gee[10], Matthew M. Haney[11], Hugo D. Ortiz[1], Quentin Brissaud[12], Léo Martire[7], Lucie Rolland[13], Panagiotis Vergados[7], Alexandra Nippress[4], Junghyun Park[14], Shahar Shani-Kadmiel[3], Alex Witsil[2], Stephen Arrowsmith[14], Corentin Caudron[15], Shingo Watada[9], Anna B. Perttu[16,17], Benoit Taisne[16,18], Pierrick Mialle[19], Alexis Le Pichon[20], Julien Vergoz[20], Patrick Hupe[21], Philip S. Blom[22], Roger Waxler[23], Silvio De Angelis[24], Jonathan B. Snively[25], Adam T. Ringler[26], Robert E. Anthony[26], Arthur D. Jolly[27], Geoff Kilgour[28], Gil Averbuch[14], Maurizio Ripepe[29], Mie Ichihara[9], Alejandra Arciniega-Ceballos[30], Elvira Astafyeva[31], Lars Ceranna[21], Sandrine Cevuard[32], Il-Young Che[33], Rodrigo De Negri[1], Carl W. Ebeling[34], Läslo G. Evers[3], Luis E. Franco-Marin[35], Thomas B. Gabrielson[36], Katrin Hafner[37], R. Giles Harrison[38], Attila Komjathy[7], Giorgio Lacanna[29], John Lyons[11], Kenneth A. Macpherson[2], Emanuele Marchetti[29], Kathleen F. McKee[39], Robert J. Mellors[34], Gerardo Mendo-Pérez[40], T. Dylan Mikesell[41], Edhah Munaibari[13], Mayra Oyola-Merced[7], Iseul Park[33], Christoph Pilger[21], Cristina Ramos[42], Mario C. Ruiz[42], Roberto Sabatini[25], Hans F. Schwaiger[11], Dorianne Tailpied[16], Carrick Talmadge[23], Jérôme Vidot[8], Jeremy Webster[22], David C. Wilson[26]

The 15 January 2022 climactic eruption of Hunga volcano, Tonga, produced an explosion in the atmosphere of a size that has not been documented in the modern geophysical record. The event generated a broad range of atmospheric waves observed globally by various ground-based and spaceborne instrumentation networks. Most prominent was the surface-guided Lamb wave (≤0.01 hertz), which we observed propagating for four (plus three antipodal) passages around Earth over 6 days. As measured by the Lamb wave amplitudes, the climactic Hunga explosion was comparable in size to that of the 1883 Krakatau eruption. The Hunga eruption produced remarkable globally detected infrasound (0.01 to 20 hertz), long-range (~10,000 kilometers) audible sound, and ionospheric perturbations. Seismometers worldwide recorded pure seismic and air-to-ground coupled waves. Air-to-sea coupling likely contributed to fast-arriving tsunamis. Here, we highlight exceptional observations of the atmospheric waves.

T he 15 January 2022 eruption of Hunga volcano (*1*), Tonga, was an unusually energetic explosive event. This climactic eruption (the largest eruption of an episode) began just after ~04:00 UTC (~17:00 local time) from a submerged vent and delivered volcanic tephra and gas primarily into the stratosphere. An umbrella cloud developed at ~30 km above sea level, with a much higher central transient overshoot. Hunga is a largely submerged massif located ~65 km to the north-northwest of Tongatapu, Kingdom of Tonga. Eruption episodes consisting of relatively low-energy Surtseyan activity in 2009 and 2014–2015 had built a tephra cone that connected the established islands of Hunga Tonga and Hunga Ha'apai on the northwestern portion of the massif (*2*). Surtseyan eruptions transitioned into violent, impulsive eruptions starting on 19 December 2021 as part of the most recent episode. The climactic 15 January eruption produced a broad range of atmospheric waves observed globally by numerous ground-based and spaceborne instrumentation systems, including atmospheric pressure sensors, seismometers, hydrophones, Global Navigation Satellite System (GNSS) receivers, and weather satellites (Fig. 1A) (*3*). Here, we highlight exceptional multi-technology observations of this extraordinary event in the modern digital record and provide initial interpretations of the atmospheric wave types generated and their propagation around the globe.

The onset of the most recent eruptive episode was characterized remotely by seismicity and co-eruptive infrasound on 19 December 2021, preceded by seismic activity on 18 December 2021 (16:49:46 UTC; body-wave magnitude: 4.0) (Fig. 1B) (*3*). Eruptive activity continued until 4 January 2022, with decreasing infrasonic amplitudes at International Monitoring System (IMS) infrasound station IS22 (1848 km range) and intermittent detections by IMS hydroacoustic stations. Powerful eruptive infrasound activity resumed on 13 January 2022, with amplitudes ~10 times that of the December activity. Infrasound continued on 14 January, accompanied by seismic tremor (*3*) (fig. S2, A and B); infrasound amplitudes subsequently decreased, while the number of hydroacoustic *T*-phase detections increased. After brief relative quiescence, at least four IMS hydroacoustic (fig. S3), all 53 IMS infrasound, and numerous seismic stations detected the main climactic eruption on 15 January 2022 [04:14:45 UTC; moment magnitude (M_w): 5.7 to 5.8; table S1]. Regional infrasound, barometer, and volcanic plume observations suggest a complex eruption sequence occurring between 04:00 and ~04:30, not just a single onset or explosion (Figs. 1A, 2E, and 3A). A final major eruption at ~08:31 UTC on 15 January was detected by at least 20 IMS infrasound and two IMS hydroacoustic stations, after which the volcanic activity decreased.

Atmospheric waves (*4*) are propagating mechanical perturbations in the atmospheric

[1]Department of Earth Science and Earth Research Institute, University of California, Santa Barbara, CA, USA. [2]Wilson Alaska Technical Center and Alaska Volcano Observatory, Geophysical Institute, University of Alaska Fairbanks, Fairbanks, AK, USA. [3]R&D Department of Seismology and Acoustics, Royal Netherlands Meteorological Institute (KNMI), De Bilt, Netherlands. [4]AWE Blacknest, Brimpton, Reading, UK. [5]Lawrence Livermore National Laboratory, Livermore, CA, USA. [6]Seismology-Gravimetry, Royal Observatory of Belgium, Brussels, Belgium. [7]NASA Jet Propulsion Laboratory (JPL), California Institute of Technology, Pasadena, CA, USA. [8]CNRM, Université de Toulouse, Météo-France, CNRS, Lannion, France. [9]Earthquake Research Institute, University of Tokyo, Tokyo, Japan. [10]Department of Physics and Astronomy, Brigham Young University, Provo, UT, USA. [11]US Geological Survey (USGS), Alaska Volcano Observatory, Anchorage, AK, USA. [12]Norwegian Seismic Array (NORSAR), Kjeller, Norway. [13]Université Côte d'Azur, Observatoire de la Côte d'Azur, CNRS, IRD, Géoazur, Sophia Antipolis, Valbonne, France. [14]Roy M. Huffington Department of Earth Sciences, Southern Methodist University, Dallas, TX, USA. [15]Laboratoire G-Time, Department of Geosciences, Environment and Society, Université libre de Bruxelles, Brussels, Belgium. [16]Earth Observatory of Singapore, Nanyang Technological University, Singapore. [17]Volcanic Risk Solutions, Massey University, Palmerston North, New Zealand. [18]Asian School of the Environment, Nanyang Technological University, Singapore. [19]Comprehensive Nuclear-Test-Ban Treaty Organization (CTBTO), Vienna, Austria. [20]CEA, DAM, DIF, Arpajon, France. [21]BGR (Federal Institute for Geosciences and Natural Resources), Hannover, Germany. [22]Geophysics Group, Los Alamos National Laboratory, Los Alamos, NM, USA. [23]National Center for Physical Acoustics, University of Mississippi, University, MS, USA. [24]School of Environmental Sciences, University of Liverpool, Liverpool, UK. [25]Department of Physical Sciences and Center for Space and Atmospheric Research (CSAR), Embry-Riddle Aeronautical University, Daytona Beach, FL, USA. [26]USGS Albuquerque Seismological Laboratory, Albuquerque, NM, USA. [27]USGS Hawaiian Volcano Observatory, Hilo, HI, USA. [28]GNS Science, Wairakei Research Centre, Taupō, New Zealand. [29]Department of Earth Sciences, University of Florence, Florence, Italy. [30]Departamento de Vulcanología, Instituto de Geofísica, Universidad Nacional Autónoma de México, Mexico City, Mexico. [31]Université de Paris, Institut de Physique du Globe de Paris, Paris, France. [32]Vanuatu Meteorology and Geohazards Department, Port Vila, Vanuatu. [33]KIGAM (Korea Institute of Geoscience and Mineral Resources), Daejeon, Korea. [34]Institute of Geophysics and Planetary Physics, Scripps Institution of Oceanography, University of California, San Diego, La Jolla, CA, USA. [35]Volcanological Observatory of the Southern Andes (OVDAS), National Geology and Mining Service (SERNAGEOMIN), Temuco, Chile. [36]Graduate Program in Acoustics, Penn State University, State College, PA, USA. [37]Incorporated Research Institutions for Seismology (IRIS), Washington, DC, USA. [38]Department of Meteorology, University of Reading, Reading, UK. [39]NASA Goddard Space Flight Center, Greenbelt, MD, USA. [40]Posgrado en Ciencias de la Tierra, Universidad Nacional Autónoma de México, Mexico City, Mexico. [41]Norwegian Geotechnical Institute (NGI), Oslo, Norway. [42]Instituto Geofísico, Escuela Politécnica Nacional, Quito, Ecuador.
*Corresponding author. Email: rmatoza@ucsb.edu

fluid. Nonlinearities in the propagation cause the spectrum to evolve (i.e., energy cascading) and may result in shock-wave formation and period lengthening. Gravity waves are disturbances to the balance between buoyancy and gravity [frequency (f) ≲ 3 mHz]; acoustic waves manifest as propagating compressions and rarefactions (f ≳ 4 mHz). These different physical mechanisms lead to different propagation speeds. Acoustic-gravity waves (AGWs) are waves exhibiting both buoyant and compressional motion (5), typically with millihertz frequencies and long wavelengths (tens of kilometers) relative to density stratification scale heights (fig. S4). Lamb waves (6) are AGWs propagating along Earth's surface, with group velocities near the mean sound speed of the lower atmosphere [~310 m/s for a 16-km scale height above Earth's surface (7)]. Lamb waves are associated with the largest atmospheric explosions from volcanic eruptions (8) and nuclear tests (9) and have periods on the order of several to hundreds of minutes. Audible sound refers to higher-frequency acoustic waves that can be heard by humans. Infrasound (10) refers to acoustic waves below the standard audio range. The crossover between audible and infrasound is often given as 20 Hz.

Of the atmospheric waves produced by the climactic Hunga explosion, the most prominent is the Lamb wave (f ≲ 0.01 Hz), which propagates efficiently and is detected globally by numerous ground-based and spaceborne geophysical instrumentation systems (Fig. 1A, fig. S5, and movies S1 to S6). Despite the Lamb wave's large amplitude, its waveform pressure increase as a function of time (rise time) is relatively slow and does not have characteristics of a shock wave. Over 6 days, we observed global propagation of at least four minor-arc Lamb wave passages (A1, A3, A5, and A7) and three (A2, A4, and A6) major-arc (antipodal) passages (Figs. 1A, inset, and 2, A and B, and fig. S6A).

The number of Lamb wave passages observed for Hunga (four, plus three antipodal) is approximately the same as observed for the 1883 Krakatau eruption (11, 12) (Fig. 2A). The exceptional spatiotemporal resolution of the evolving wavefield from 2022 Hunga, in comparison with 1883 Krakatau, is a consequence of more than a century of advances in instrumentation technology and global sensor density (Fig. 1A). Measurements of Lamb wave peak-to-peak pressure amplitudes as a function of distance indicate that the atmospheric pressure pulse generated by the Hunga event is comparable to that of the 1883 Krakatau eruption (12) (Fig. 2F and fig. S8). However, the duration of the Krakatau Lamb pulse was ~30% longer than that of Hunga at comparable stations (Fig. 2A). Peak-to-peak pressure amplitudes from Hunga generally decreased logarithmically from 1473 Pa (756 km) with increasing distance (range) from the source (Fig. 2F and fig. S9). We infer that the notable

scatter in amplitudes at distances >7500 km is related to winds and wavefront focusing around the spherical Earth (3) and to a potentially anisotropic source. The Hunga signal amplitudes are more than an order of magnitude larger than those generated by the 1980 Mount St. Helens eruption (13).

Equivalent explosive yields for large volcanic eruptions have previously been estimated using pressure recordings, but quantitative comparisons with nonvolcanic sources are problematic. During the atmospheric nuclear testing era of the 1950s and 1960s, theoretical and empirical relationships were generated relating AGW amplitudes and periods to explosive yield (14, 15). We find that such relationships are inapplicable to the signals generated by Hunga, as they result in unphysically large equivalent yields (3) (fig. S10A). This difference is presumably because, for a given energy release, the long-duration climactic eruption excites longer-period pressure disturbances than the near-instantaneous nuclear reaction (fig. S10B). Hunga signals have peak-to-peak pressures comparable to those produced by the largest historical atmospheric nuclear test (58 megatons, USSR, 1961) (16), but the dominant eruption signal periods (1700 to 2500 s) are approximately four times longer than those of the anthropogenic explosion (400 to 700 s) (17).

The Hunga eruption pressure waves have complex waveform and spectral characteristics, likely related to both source and propagation.
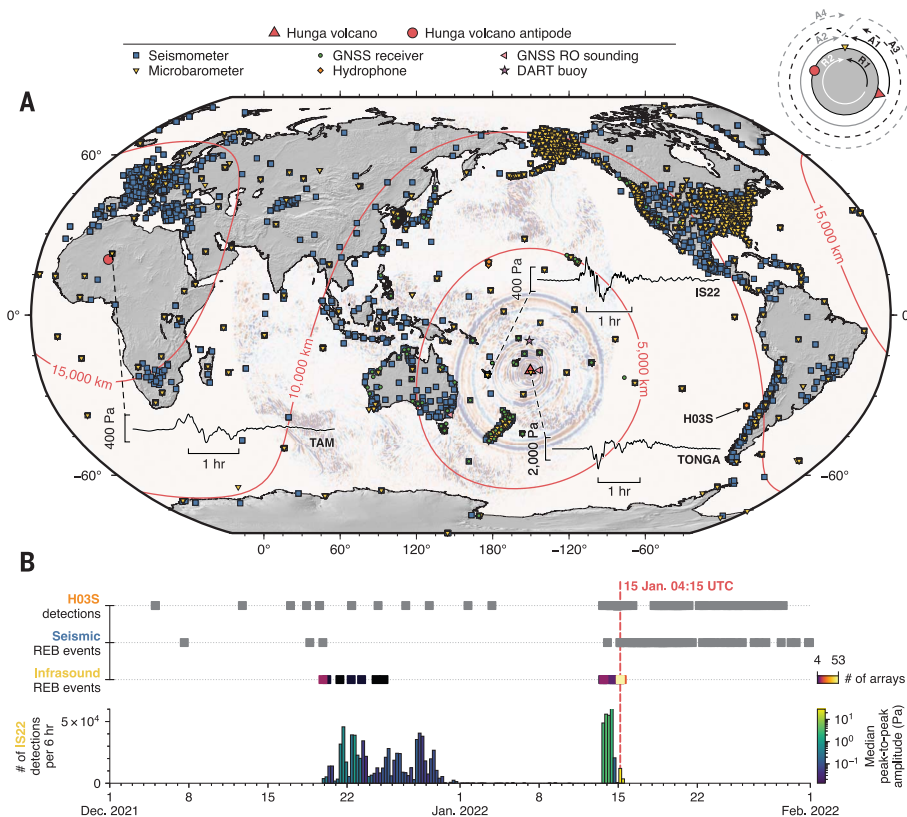

Fig. 1. Global distribution of recording geophysical sensors used in this study and remotely observed eruption chronology. (**A**) Sensor map. Background image is brightness temperature difference (Himawari-8) at 07:10 UTC on 15 January 2022. Selected 4-hour pressure waveforms are filtered from 10,000 to 100 s. Upper-right inset shows Hunga wave paths around Earth. (**B**) Hunga activity, December 2021 through January 2022, observed at IMS hydrophone, seismic, and infrasound stations (REB, Reviewed Event Bulletin); Hunga detections from nearest IMS infrasound array IS22 (1848 km). Frequency responses for atmospheric pressure sensors used in this study are displayed in fig. S1.

Fig. 2. Ground-based observations.
(**A**) Lamb wave arrival times for 2022 Hunga eruption (black) compared with 1883 Krakatau eruption (blue). (Inset) Lamb A1 arrival waveform comparison (*3*). Global record sections of (**B**) barometer, (**C**) infrasound, and (**D**) seismic data showing the multiple arrivals and wave passages (see Fig. 1A, inset); waveforms aggregated by radial distance (fig. S7). A separate Rayleigh R1 is associated with the later ~08:31 event. (**E**) Colocated microbarometer (black), infrasound sensor (blue), and seismometer (orange) waveforms; lower panel shows inverted displacement envelope. (**F**) Wideband peak-to-peak pressure versus distance comparing 2022 Hunga with large historical explosive events (table S2).
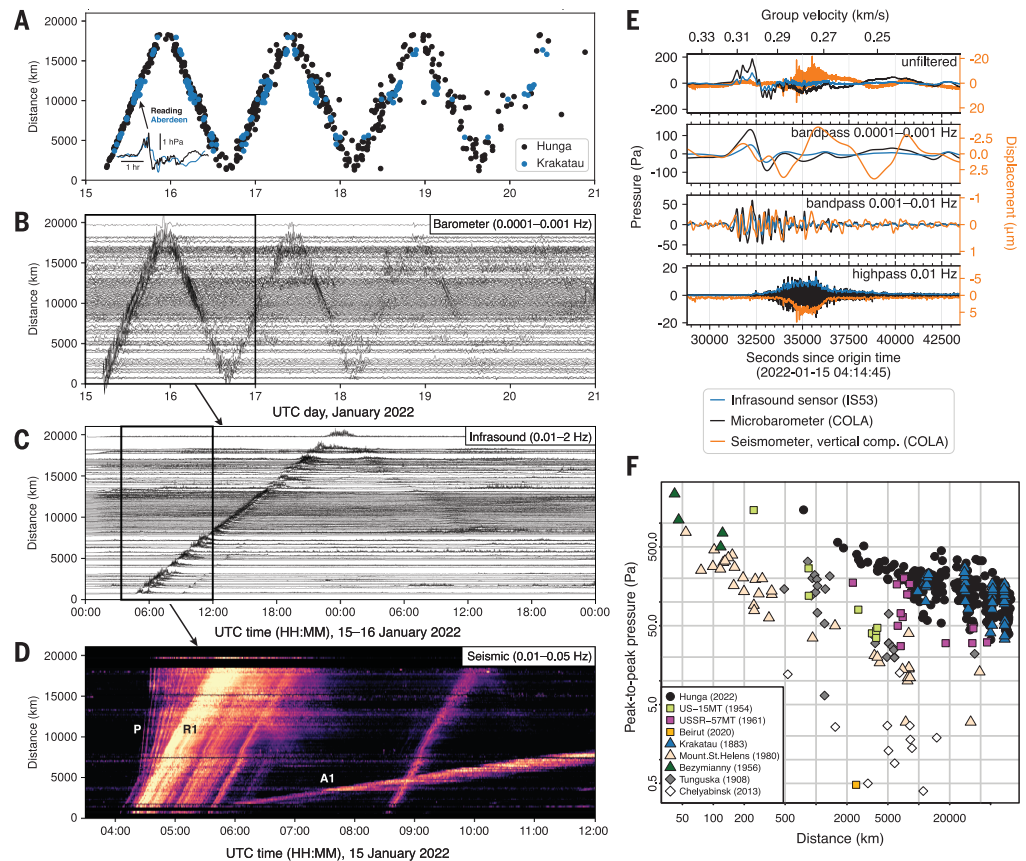
The Lamb wave is the largest-amplitude pressure wave arrival (Fig. 2B) (*3*). Near Hunga, the Lamb wave consists of at least two pulses and begins with a 7- to 10-min pressure increase, followed by a second larger compression and subsequent long rarefaction phase (Figs. 1A and 2). This sequence is different from a single bipolar pulse typical of large anthropogenic explosions (*18*). The shallow-submarine volcanic source presumably contributes to this waveform complexity (*19*). The Lamb wave period ranges from 0.3 to 10 mHz (3300 to 100 s), and the group velocity is ~315 m/s (*3*, *20*) (fig. S11). Each subsequent antipodal passage produces an observed 90° phase shift in the Lamb wave (*21*) (fig. S12). This 90° phase shift is expected given the comparison of the asymptotic forms of the equation for a traveling wave on the surface of a sphere from before the antipodal crossing to that from after crossing (*21*, *22*). The Lamb wave is composed of several AGW modes, and the Hunga signals show distinct dispersion at higher frequencies (fig. S13), which was similarly noted for other large AGW signals (*20*). Some barometer observations also show the arrival of a lower-velocity gravity wave (figs. S11 and S14).

The climactic Hunga eruption also produced remarkable long-range infrasound (f ~ 0.01 to 20 Hz), clearly detected at most IMS infrasound arrays (fig. S15) and at numerous regional arrays and networks (*3*) (table S4 and figs. S16 to S21). Infrasound signals arrive after the Lamb wave; at most stations, the Lamb wave dominates below ~0.01 Hz, followed by broadband infrasound (Fig. 3). The IMS infrasound network recorded at least two direct and two antipodal infrasonic wave arrivals from the main explosive event. At most of the infrasound stations, array processing indicates direct infrasonic arrivals for ~2 hours, with group velocities between 250 and 290 m/s (*3*) (fig. S15). Infrasound amplitudes after the first Lamb wave arrival A1 are on the order of several pascals and are observed to decrease with each global wave passage (Fig. 2F). Complex waveform interference effects are observed for stations near the source and the antipode, where the wavetrains of successive arrivals overlap (*3*). Prominent time evolution in signal backazimuth and apparent velocity is observed at many infrasound arrays, especially at stations for which the propagation path crosses the circumpolar vortex (*3*) (fig. S22).

Accounts of audible sound (f > 20 Hz) were reported across Alaska as far as 10,000 km from Hunga [compared with ~4800 km for the 1883 Krakatau eruption (*12*)] and are verified by ~30-min-duration signals on higher-sample-rate low-frequency microphone stations (Fig. 3E). The audio signals arrive after the Lamb wave and at the end of the infrasound wavetrain and consist of short-duration impulsive signals consistent with repeated "booms" reported by observers. Linear propagation and attenuation models cannot explain the high-frequency infrasound and audible sound at these extreme ranges, implying nonlinearity in generating the higher frequencies along the propagation path (*3*, *13*). Evidence of nonlinearity in Fig. 3E is twofold. First, the high-frequency spectral slope during the "peak" time window approximates that of an ideal shock wave in its old-age (*3*) (but still nonlinear) decay: f^{-2}, followed by a faster exponential roll-off at frequencies where atmospheric absorption dominates nonlinearity. Second, the impulsive events, when separated from the lower-frequency, higher-amplitude infrasound portion by filtering (from 10 to 40 Hz), have coarsely sampled *N*-wave shapes reminiscent of explosions or sonic booms. Substantial increases in global population and advances in societal connectivity (e.g., internet versus telegraph) presumably contribute to the enhanced reports of audibility at distances greater than those historically documented for Krakatau and other large events.

Owing to its extraordinary amplitude, the Lamb wave produced coupled signals at multi-technology stations (Fig. 2E) (*3*). For example,

in the Mediterranean, the Lamb wave produced signals on hydrophones at ~50 m water depth near Stromboli volcano, 17,740 km from Hunga (*3*) (fig. S17B).

Seismometers worldwide recorded ground motions associated with both pure seismic waves (figs. S2 and S23) and air-to-ground coupled atmospheric waves (Fig. 3 and figs. S24 and S6B). We associate the most prominent seismic (*P*, *S*, and Rayleigh waves) and atmospheric arrivals (Fig. 2) with the main eruption at 04:14:45 UTC, which had a reported M_w of between 5.7 and 5.8. Our observations of multiple overlapping seismic phases (Fig. 2D) suggest a longer-duration source process, with at least two discrete events and multiple phases. Additionally, seismic ground motions glob-

ally exhibit a marked spectral peak at 3.7 mHz (Fig. 3D). We interpret this peak as Rayleigh-wave propagation (corresponding to Earth normal mode $_0S_{29}$) resulting from the coupling of fundamental acoustic mode oscillations of the atmosphere near the volcanic source into the solid Earth (*3*) (fig. S25). This solid Earth mode was also excited during the 1991 eruption of Mount Pinatubo (*23*); however, the seismic oscillations generated by the climactic 2022 Hunga eruption are more than an order of magnitude larger (*3*).

Numerous additional Earth observation systems recorded the atmospheric waves from the climactic eruption. Data from neutral atmospheric radio occultations (ROs), satellite-based radiometers, and dual-frequency GNSS

receivers, in conjunction with data from ground-based infrasound stations and a DART (Deep-ocean Assessment and Reporting of Tsunamis) buoy (1225 km), reveal strong seismo- and hydroatmospheric coupling in the aftermath of the eruption (Fig. 4). The Lamb wave arrival time at IS-II (station CTAO, 3997 km) is consistent with that obtained using brightness temperature differences measured by the Himawari-8 satellite (*3*) (fig. S5). At this time, an RO profile over Eastern Australia (RO-III, 3781 km) clearly displays heightened gravity wave activity in the stratosphere. In the hours after the eruption, ROs in the vicinity of Hunga (RO-I, 366 km, and RO-II, 453 km) also reveal strong gravity wave activity in the stratosphere with temperature perturbations of ±4 K, four times the typical background activity.

The atmospheric waves also propagated to the ionosphere, where 1 Hz data recorded in real time by ground-based GNSS stations can be converted to ionospheric total electron content (TEC). TEC data clearly demonstrate wave-like structures of unprecedented magnitude traveling between ~320 and 1000 m/s. TEC profiles (G-I and G-II) collocated with infrasound stations IS-I (station MSVF, 756 km) and IS-II show the arrival of the Lamb wave in the ionosphere ~24 min after it is recorded at the infrasound station (propagating at an apparent vertical velocity of ~312 m/s for an assumed ionospheric shell height of 450 km). As in the global barometer data (Fig. 2B), the Lamb wave was observed worldwide in TEC data. In addition, a DART buoy (B-I) and a nearby TEC record (G-III) north of Hunga record tsunami-like waves generated by the atmospheric pulse [i.e., air-sea waves (*8*)], 1 hour before the appearance of tsunami signatures of direct volcanic origin (*3*) (fig. S26).

Understanding these geophysical observations from the Hunga eruption requires accurate propagation modeling. However, simulating atmospheric wave propagation is challenging here for multiple reasons. (i) The complexity of the highly energetic, shallow-submarine, and multiphase eruption is beyond existing capability for modeling the source and the subsequent repartition of energy among the different waves (*3*). (ii) The physical problem involves multiple scales. Indeed, observed atmospheric waves contain energy extending from the acoustic-gravity regime, including a strong Lamb wave, through the infrasonic range, and into audio frequencies (Fig. 3). (iii) Atmospheric wave propagation is strongly nonlinear, which leads to energy cascading into higher frequencies even far from the event. For such energetic events, wave propagation nonlinearities remain important far from the source. Considering (ii) and (iii) together, the challenge is due to the nonlinear energy cascading that couples these various regimes (acoustic-gravity, infrasound, audio)
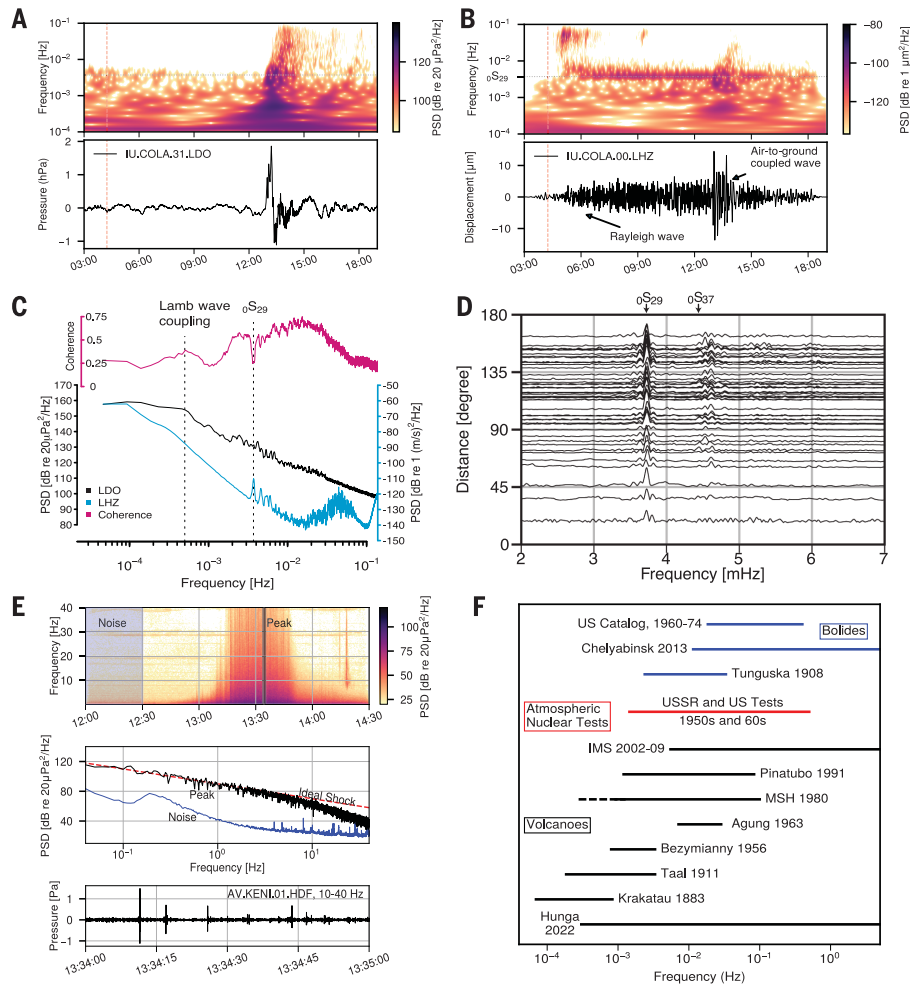

Fig. 3. Seismoacoustic spectral properties. Colocated wideband (**A**) pressure and (**B**) seismic spectrograms (top) and unfiltered waveforms (bottom). (**C** and **D**) Power spectral densities (PSD) and seismoacoustic coherences worldwide show that pressure waves couple to the solid Earth through both (i) direct conversion as the Lamb wave passes the station and (ii) near-source excitation of atmospheric acoustic modes. (**E**) Alaska infrasound stations recorded audio range signals at great distances, apparent in the spectra (top) and as intermittent transients with shock-like features (middle and bottom panels). (**F**) Observed wideband pressure spectral character of the Hunga eruption compared with published instrumental observations of previous events (table S3).
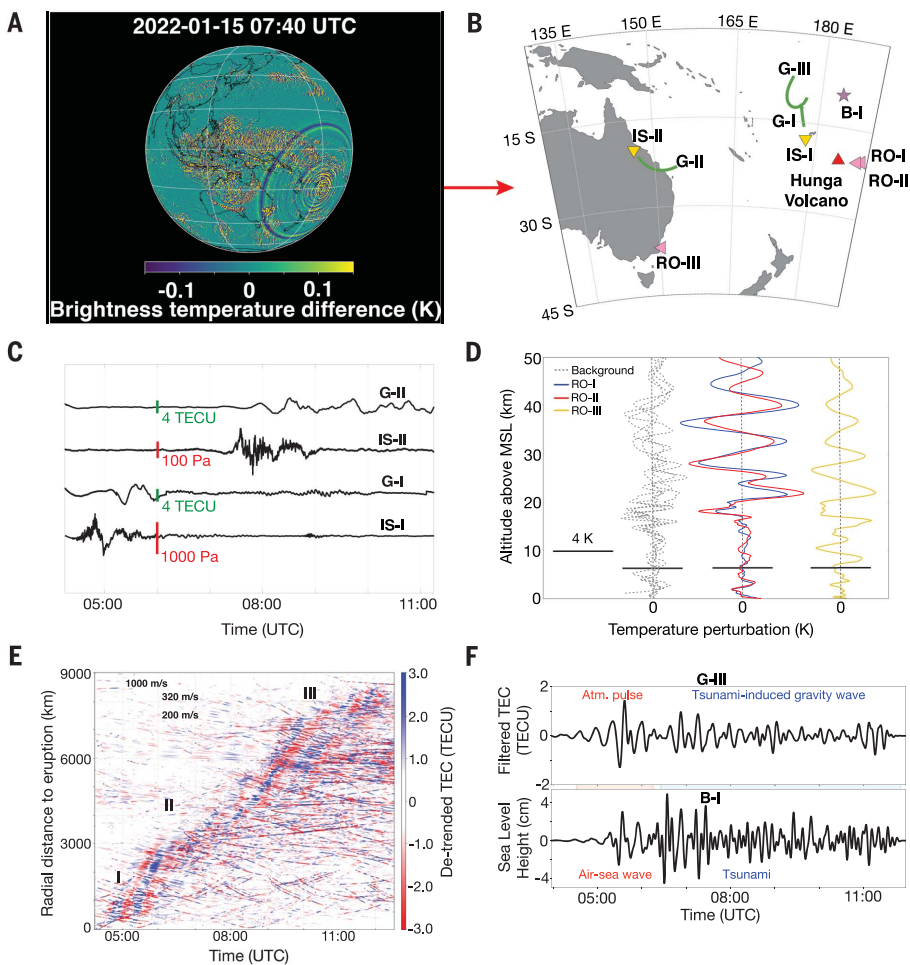
Fig. 4. Seismo- and hydroatmospheric coupling from Earth's surface to space. (**A**) Brightness temperature variations in Himawari-8 data showing waves emanating from the Hunga eruption site. (**B**) Map of the inset in (A), with measurement locations in this figure. Ionospheric pierce point arcs (see supplementary materials section 1.13) are shown in green for the Lamb wave arrival for links G-I and G-II, and from 04:00 to 12:00 UTC for link G-III. (**C**) Infrasound (stations IS-I and IS-II) and TEC (GNSS links G-I and G-II) waveforms showing Lamb wave arrival; all signals high-pass filtered with 0.278 mHz (corresponding to 1-hour period) cutoff. (**D**) RO-I and RO-II at 06:50 UTC and 10:00 UTC showing strong coherent gravity wave activity several hours after the eruption; RO-III at 07:42 UTC also exhibits large gravity waves coincident with Himawari-8 data (A). (**E**) Hodochron plot of TEC records showing long-distance ionospheric wave propagation after the eruption. Features I and II are the first arrivals with different apparent wave velocities (551 to 1333 m/s) due to the near-field wavefront curvature. Feature III, identified more than 6000 km from the eruption, propagates at 478 m/s and is more likely linked to long-period gravity waves. (**F**) Buoy B-I data compared with TEC data from an adjacent GNSS link (G-III) showing efficient air-sea-air coupling across a broad frequency spectrum (3).

and requires modeling methods that account for that coupling. (iv) Finally, substantial temporal and spatial variations of atmospheric conditions along propagation paths render a stratified atmospheric model inappropriate. Existing propagation algorithms [based, for instance, on the equations of fluid mechanics, the parabolic approximation of the wave equation, normal-mode summation, or ray tracing (3)] are limited in their physics and computational feasibility (fig. S27). Nevertheless, preliminary simulations (3) find notable departures of predicted propagation paths from great circle paths (fig. S28 and movie S7), which leads to direction-of-arrival deviations qualitatively in agreement with observations (fig. S22 and table S5).

The impacts of volcanic atmospheric waves are usually limited, but sometimes shock waves from strong volcanic explosions damage nearby infrastructure (24, 25). Atmospheric waves from the main Hunga eruption had far more extensive effects. Unusual sea level changes or tsunamis were observed in the Pacific earlier than predicted, as well as in the Caribbean and Mediterranean without direct ocean routes. We report observations of early sea level oscil-lations in the Pacific (3). At coastal tide gauges, the tsunami onset time approximately coincides with the Lamb wave arrival (2 hPa pulse); the tsunami onset is unclear, but wave amplitudes gradually increase over 2 to 4 hours to >1 m in some locations. In contrast, deep-sea tsunami-meters record a clear leading 5 hPa pressure pulse, more than double that of the air-pressure pulse (3) (figs. S29 and S30). Air-sea coupling (8, 26) likely caused these exceptional observations and should be considered in future scenarios for tsunami early-warning systems.

Geophysical records of the January 2022 Hunga eruption represent an unparalleled global dataset of atmospheric wave generation and propagation, providing an opportunity for multi-technology observation, modeling, and validation that is unprecedented in the modern record. The datasets highlighted here are not exhaustive; there is outstanding potential for augmenting details of the global wavefield capture by incorporating numerous additional interdisciplinary datasets, including citizen-science data (27, 28). The January 2022 Hunga eruption presents an extraordinary opportunity to advance understanding of rarely captured physical phenomena, including global Lamb wave propagation, atmospheric free-oscillations coupling with the solid Earth, nonlinear energy cascading in atmospheric wave propagation, excitation of infrasound and audible sound at global distances, air-sea waves, and many others.

REFERENCES AND NOTES

1. The name of the volcano is "Hunga," not "Hunga Tonga." "Hunga" refers to the entire volcano, rather than the islands. "Hunga Tonga" refers specifically to the most southwestern of the two islands.
2. R. G. Vaughan, P. W. Webley, *J. Volcanol. Geotherm. Res.* **198**, 177–186 (2010).
3. Materials and methods and data and network citations are available as supplementary materials.
4. E. E. Gossard, W. H. Hooke, *Waves in the Atmosphere: Atmospheric Infrasound and Gravity Waves—Their Generation and Propagation* (Elsevier, 1975).
5. K. C. Yeh, C. H. Liu, *Rev. Geophys.* **12**, 193–216 (1974).
6. H. Lamb, *Proc. R. Soc. London Ser. A* **84**, 551–572 (1911).
7. F. P. Bretherton, *Q. J. R. Meteorol. Soc.* **95**, 754–757 (1969).
8. D. Harkrider, F. Press, *Geophys. J. Int.* **13**, 149–159 (1967).
9. A. D. Pierce, J. W. Posey, *Geophys. J. R. Astron. Soc.* **26**, 341–368 (1971).
10. R. Matoza, D. Fee, D. Green, P. Mialle, in *Infrasound Monitoring for Atmospheric Studies: Challenges in Middle Atmosphere Dynamics and Societal Benefits*, A. Le Pichon, E. Blanc, A. Hauchecorne, Eds. (Springer, Cham, 2019), pp. 1023–1077.
11. R. H. Scott, *Proc. R. Soc. London* **36**, 139–143 (1883).

12. R. H. Strachey, in *The Eruption of Krakatoa and Subsequent Phenomena*, Report of the Krakatoa Committee of the Royal Society, G. J. Symons, Ed. (Trübner and Co., 1888).
13. J. W. Reed, *J. Geophys. Res.* **92**, 11979–11992 (1987).
14. J. W. Posey, A. D. Pierce, *Nature* **232**, 253–253 (1971).
15. G. B. Olmsted, "Detection of airborne low-frequency sound from nuclear explosions," United States Air Force, Office for Atomic Energy, Operation Castle Report WT-931 (1955)
16. W. L. Donn, D. M. Shaw, A. C. Hubbard, *IEEE Trans. Nucl. Sci.* **10**, 285–296 (1963).
17. A. D. Pierce, C. A. Moo, J. W. Posey, "Generation and propagation of infrasonic waves," Air Force Cambridge Research Laboratories, AFCRL-TR-73-0135 (1973).
18. D. Fee *et al.*, *J. Geophys. Res. Atmos.* **118**, 6122–6143 (2013).
19. J. J. Lyons, M. M. Haney, D. Fee, W. G. Wech, C. F. Waythomas, *Nat. Geosci.* **12**, 952–958 (2019).
20. F. Press, D. Harkrider, *J. Geophys. Res.* **67**, 3889–3908 (1962).
21. J. N. Brune, J. E. Nafe, L. E. Alsop, *Bull. Seismol. Soc. Am.* **51**, 247–257 (1961).
22. J. H. Ansell, *Geophys. J. Int.* **32**, 95–117 (1973).
23. S. Watada, H. Kanamori, *J. Geophys. Res.* **115**, B12319 (2010).
24. K. Kato, H. Yamasato, *Earth Planets Space* **65**, 2 (2013).
25. G. A. Valentine, *J. Volcanol. Geotherm. Res.* **87**, 117–140 (1998).
26. J. Proudman, *Geophys. Suppl. Mon. Not. R. Astron. Soc.* **2**, 197–209 (1929).
27. A. M. Portas, L. Barnard, C. Scott, R. G. Harrison, *Philos. Trans. R. Soc. London Ser. A* **374**, 20150223 (2016).
28. E. Calais *et al.*, *Science* **376**, 283–287 (2022).

ACKNOWLEDGMENTS

SUPPLEMENTARY MATERIALS